

How Much of Monthly Subsurface Temperature Variability in the Equatorial Pacific Can Be Recovered by the Specification of Sea Surface Temperatures?

ARUN KUMAR

NOAA/NWS/NCEP/Climate Prediction Center, College Park, Maryland

HUI WANG

NOAA/NWS/NCEP/Climate Prediction Center, College Park, Maryland, and Wyle Science, Technology and Engineering Group, Houston, Texas

YAN XUE AND WANQIU WANG

NOAA/NWS/NCEP/Climate Prediction Center, College Park, Maryland

(Manuscript received 30 April 2013, in final form 26 August 2013)

ABSTRACT

The focus of the analysis is to investigate the question to what extent the specification of sea surface temperature (SST) in coupled model integration can impart realistic evolution of subsurface ocean temperature in the equatorial tropical Pacific. In the context of El Niño–Southern Oscillation (ENSO) prediction, the analysis is of importance from two aspects: such a system can be considered as a simple coupled ocean data assimilation system that can provide ocean initial conditions; and what additional components of the ocean observing system may be crucial for skillful ENSO prediction.

The results indicate that coupled model integration where SST is continuously nudged toward the observed state can generate a realistic evolution of subsurface ocean temperature. The evolution of slow variability related to ENSO, in particular, has a good resemblance against the observational counterpart. The realism of subsurface ocean temperature variability is highest near the date line and least in the far eastern Pacific where the thermocline is shallowest. The results are also discussed in the context of ocean observing system requirements for ENSO prediction.

1. Introduction

Skill of long-range predictions (e.g., seasonal and decadal) resides in initializing the ocean that provides the long-term memory and skillful predictions for sea surface temperature (SST; Jin et al. 2008; Xue et al. 2013; Meehl et al. 2014). Skillful prediction of SST anomalies, an example being SST variability related to El Niño–Southern Oscillation (ENSO), by controlling various aspects of global atmospheric and terrestrial climate variability, also allows us to make skillful prediction of variables of societal relevance (e.g., surface temperature and precipitation; Ropelewski and Halpert 1986; Trenberth et al. 1998; Peng et al. 2012).

For the initialization of ocean conditions, a hierarchy of procedures with varying complexity have been used. One of the simplest approaches has been the specification of SSTs (or SST anomalies) as the only observed information in coupled model integrations (Chen et al. 2004; Tang and Kleeman 2004; Keenlyside et al. 2005; Luo et al. 2008; Keenlyside et al. 2008) to spin up the ocean initial state. The rationale for these initialization procedures is that over regions where ocean variability is strongly constrained by coupled air–sea interaction, specified SSTs force the surface wind variability, which in turn, leads to subsurface ocean variability that resembles the observed subsurface evolution. Oceanic variability in the equatorial tropical Pacific is such a region of coupled air–sea interaction. Indeed strong coupling between ocean and atmosphere has been the basis of hybrid coupled models for the tropical Pacific that not only provided improved understanding of ENSO dynamics, but also led to the development of earlier generations of

Corresponding author address: Dr. Arun Kumar, NOAA/Climate Prediction Center, 5830 University Research Court, NCWCP, College Park, MD 20740.
E-mail: arun.kumar@noaa.gov

ENSO prediction models (Latif and Villwock 1990; Barnett et al. 1993; Balmaseda et al. 1994; Chen et al. 2004).

In this paper, based on coupled model simulations, we quantify to what extent the specification of SSTs, particularly in the equatorial tropical Pacific can reproduce the evolution of subsurface ocean temperature variability. The design of coupled model simulation is similar to the traditional approach of specification of SSTs and quantifying their influence on the atmospheric variability using the Atmospheric Model Intercomparison Project (AMIP) simulations (Peng et al. 2000; Kumar et al. 2001); however, in this case we extend the analysis to investigate how SST controls the subsurface temperature variability based on an ensemble of coupled model simulations. We investigate the question that with the specification of SSTs, what features of observed subsurface ocean temperature variability can be reproduced.

The analysis presented in this paper also has implications for the design of the ocean observing system in the equatorial tropical Pacific to adequately resolve the observed evolution of ocean variability. Over the regions where the specification of SST and coupled air–sea interactions can lead to adequate representation of ocean subsurface variability, a sparse network of ocean observing system may be adequate. On the other hand, regions where the specification of SST is inadequate in replicating subsurface ocean variability, independent ocean observations will be critical. However, in the context of prediction of ENSO variability, the question of adequacy of the ocean observing system to resolve equatorial Pacific Ocean variability may differ from the question of which region observations are crucial for initializing the ocean state for skillful prediction of ENSO-related SSTs.

The design of coupled model simulations is described in section 2 and results, including comparison with the observed ocean variability, are presented in section 3. A discussion on the implications for the ocean observing system is given in section 4, and a summary is given in section 5. With ENSO being one of the strongest modes of coupled variability in global oceans, and the very basic premise of successful seasonal prediction efforts (Peng et al. 2012), the focus of analysis is for subsurface ocean variability in the equatorial tropical Pacific.

2. Data and model simulations

The observational data used in this study include 10-m zonal wind, SST, and subsurface ocean temperature. The 10-m zonal wind data are from the National Centers for Environmental Prediction (NCEP)–Department of Energy (DOE) Reanalysis 2 (R2; Kanamitsu et al. 2002)

on a T62 Gaussian grid. The SST dataset is the National Oceanic and Atmospheric Administration (NOAA) Optimum Interpolation SST (OISST) version 2 (Reynolds et al. 2002) on a $1^\circ \times 1^\circ$ (latitude \times longitude) grid. The subsurface ocean temperatures are from both the NCEP Global Ocean Data Assimilation System (GODAS; Behringer and Xue 2004) on a $1^\circ \times 2^\circ$ grid and the European Centre for Medium-Range Weather Forecasts (ECMWF) Ocean Reanalysis System 4 (SYS4; Balmaseda et al. 2013) on a $1^\circ \times 1^\circ$ grid. The data cover a 31-yr period from 1981 to 2011.

The coupled model employed in this study is the early version of the Climate Forecast System (CFS) that was implemented for operational seasonal forecast at NCEP in 2004 (Saha et al. 2006) and was replaced by a new version in 2012 (Saha et al. 2014). In this version of the CFS, the atmospheric, oceanic, and land components of the coupled model are the NCEP Global Forecast System (GFS) version 1 (Moorthi et al. 2001), the Geophysical Fluid Dynamics Laboratory (GFDL) Modular Ocean Model version 3 (MOM3; Pacanowski and Griffies 1998), and the Oregon State University (OSU) land surface model (LSM; Pan and Mahrt 1987), respectively.

The atmospheric component (i.e., the GFS) has T62 horizontal resolution and 64 vertical levels. The GFDL MOM3 covers global oceans from 74°S to 64°N , with horizontal resolutions of 1° (longitude) by $\frac{1}{3}^\circ$ (latitude) between 10°S and 10°N , and increasing to 1° (latitude) poleward of 30°S and 30°N . The MOM3 has 40 layers from 5 m below sea level to 4479 m, with a 10-m resolution in the upper 240 m. The OSU LSM has two soil layers: 0–10 and 10–190 cm. More detailed descriptions of the CFS are given in Saha et al. (2006).

The GODAS is based on GFDL MOM3 ocean model as described above and is forced by the momentum, heat, and freshwater (evaporation minus precipitation) fluxes from R2. These surface fluxes were further corrected by restoring the model temperature of the first layer (5 m) toward the OISST analysis. A three-dimensional variational data assimilation (3DVAR) analysis scheme (Behringer et al. 1998) is used to correct model fields with in situ observations. The observed temperature data from XBTs, fixed mooring arrays including the Tropical Atmosphere Ocean/Triangle Trans-Ocean Buoy Network array (TAO/TRITON) and Argo floats are assimilated in GODAS.

To specify SST in the coupled model simulations, model SSTs are relaxed to the observed daily SST. This is done by replacing the model-predicted global SST with new SST after a 1-day integration of the coupled model. The new SST (SST_{NEW}) is a combination of the coupled model predicted SST (SST_{MOM3}) and the observed daily SST (SST_{OBS}) interpolated from the weekly OISST based on the following equation:

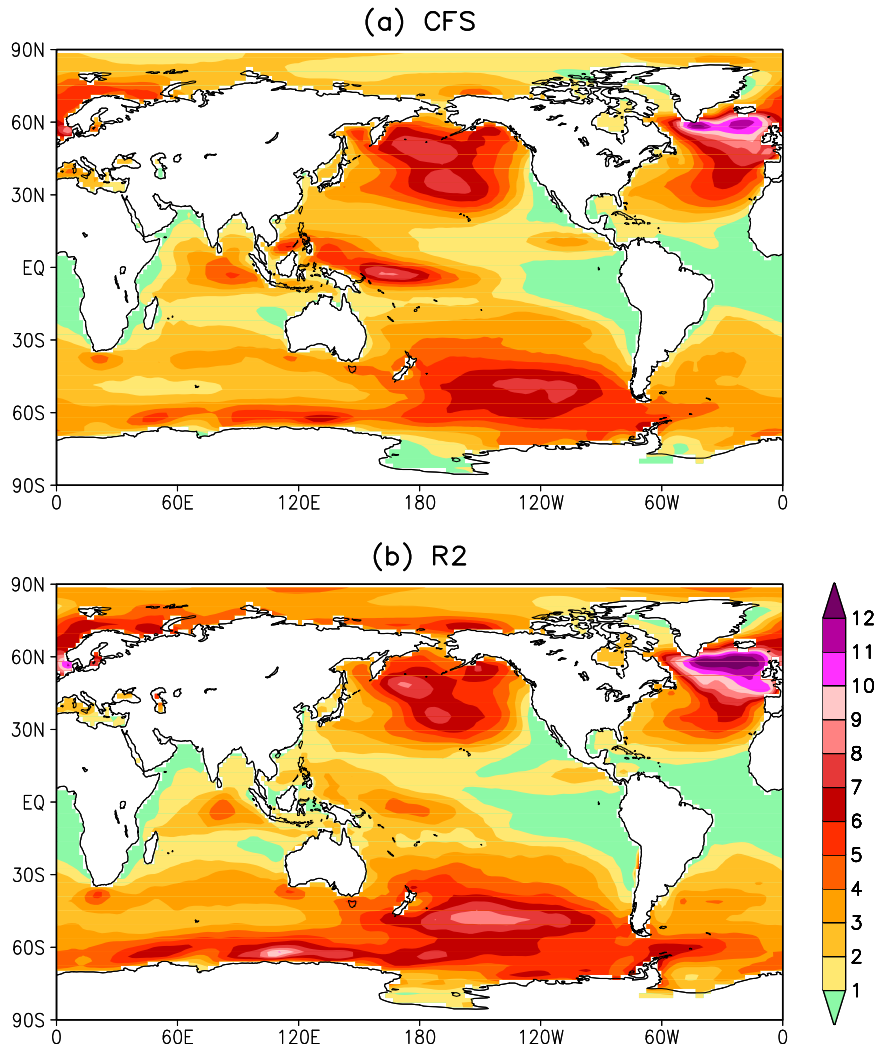


FIG. 1. Variance of monthly mean 10-m zonal wind computed over 1981–2011 (unit: $\text{m}^2 \text{s}^{-2}$). Average of (a) nine individual CFS simulations and (b) for R2.

$$\text{SST}_{\text{NEW}} = (1 - w)\text{SST}_{\text{MOM3}} + w\text{SST}_{\text{OBS}},$$

where w is a weighting coefficient, which is set to $1/3$. The value of $1/3$ for the weighting coefficient, equivalent to nudging the model SST to the observed SST with a restoring time scale of 3.3 days, effectively constrains SST_{NEW} to the observations. We point out that the SST nudging method used here differs from the SST anomaly nudging procedure (Oberhuber et al. 1998). Although of interest is whether SST or SST anomaly nudging performs better in replicating the observed ocean variability, and which nudging methodology may produce less initial shock during subsequent coupled forecasts, our focus is solely on the analysis of ocean variability resulting from the application of the SST nudging procedure alone.

The modified CFS with relaxation of the model-predicted SST to the observed global SST was integrated over the 31-yr period (1981–2011) with one ocean initial condition but nine different atmospheric initial conditions. The ocean model was initialized with 1 January 1981 condition obtained from the GODAS. The atmospheric model was initialized with 28 December 1980–5 January 1981 conditions, each 1 day apart, obtained from the NCEP/DOE R2 (Kanamitsu et al. 2002). This procedure results in an ensemble of nine simulations in which the SST variability over global oceans follows the observed SST evolution. Hereafter these simulations are referred to as CFS simulations. This set of the CFS simulations has been used to study the predictability of seasonal-mean precipitation over the tropical Indian Ocean (Chen et al. 2012) and is similar

to the set of simulations with relaxation of tropical Pacific SST only to observations in the CFS (Wang et al. 2013).

3. Results

Postulating that the influence of specified SST is communicated to the subsurface ocean primarily via surface wind variability generated by coupled air–sea interactions in response to SSTs, we begin with a comparison of monthly surface wind variability between model simulations and observations. An assessment of variance of monthly mean 10-m zonal wind between model simulations and observations based on R2 (which was used as the surface forcing in GODAS) computed over all months is shown in Fig. 1. Overall the spatial structure of variance compares well with the largest variability occurring over midlatitude oceans associated with preferred geographical locations of storm tracks (Blackmon 1976). In tropical latitudes, for both model simulations and observations, the largest variance is found over the warm pool region over the equatorial tropical Pacific extending over the eastern Indian Ocean, with a minimum in the equatorial eastern Pacific and Atlantic.

The fraction of variability in surface zonal winds that is related to specified SSTs can be estimated from the analysis of variance of ensemble mean of model simulations (Kumar and Hoerling 1995). Variability of surface winds in ensemble mean is due to specified SSTs that are common to all simulations. The signal-to-noise ratio (SNR) in zonal wind due to SSTs is then defined as the ratio of variance of ensemble mean to the total variance and is shown in Fig. 2. Larger values for SNR indicate that variability of 10-m zonal wind is constrained by interannual variations in SSTs; on the other hand small values of SNR signify that the variability is mostly due to internal variations related to atmospheric noise (Kumar and Hoerling 1995).

The largest SNR values are located in tropical latitudes, and in particular, near the date line in the equatorial tropical Pacific. Although the interannual variability in 10-m zonal wind over midlatitude oceans is large (Fig. 1, top panel), it is not related to specified SSTs, and therefore, in the coupled model simulations is mostly due to atmospheric internal variability. A general feature of SNR is that with the largest values in equatorial latitudes, its amplitude decreases poleward, and further, this behavior is similar to that of SNR analysis for upper-level heights or for precipitation (Peng et al. 2000).

The SNR analysis for model simulations cannot be compared with an observational counterpart as only a single observed realization exists. However, as the highest SNR is found over the regions associated with ENSO

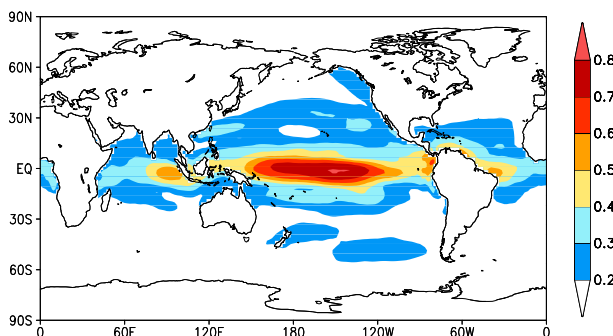


FIG. 2. Signal-to-noise ratio (SNR) for monthly mean 10-m zonal wind based on CFS simulations. The signal is the variance of the ensemble mean of nine simulations while noise is defined as the total variance.

SST variability, a comparison of linear response in surface zonal winds to ENSO SST variability between model simulations and observations can be made. This choice of comparing linear regression based on ENSO SST is also justified based on the fact that in equatorial latitudes variance of monthly mean SST associated with ENSO variability has the largest amplitude (Deser et al. 2010) and represents the strongest SST forcing for atmospheric variability on an interannual time scale.

A comparison of linear regression between the monthly mean Niño-3.4 SST index and 10-m zonal wind is shown in Fig. 3 and signifies linear response in surface zonal wind to interannual SST variability related to ENSO. Both for observations and model simulations, the largest regression is found at the equator and near the date line, and further, is located west of the largest SST anomalies; a feature also documented in earlier studies (Kumar and Hu 2012). The sign of zonal wind regression is for the westerly wind anomaly to be associated with a positive phase of Niño-3.4 SST index (i.e., El Niño events). To the west of the westerly wind anomaly, and over the eastern Indian Ocean, the zonal wind anomaly has an easterly phase and is consistent with surface divergence associated with suppressed precipitation over Indonesia that is typically associated with El Niño events (Ropelewski and Halpert 1987; Peng et al. 2000). In the meridional direction, the zonal wind anomaly has a banded structure of alternating negative and positive phases extending poleward in both the hemispheres and is indicative of surface manifestation of wave response to El Niño events emanating and propagating from tropical to extratropical latitudes (Horel and Wallace 1981; Hoerling and Kumar 1997). The amplitude and spatial structure of the linear response in surface zonal wind between observations and model simulations has a remarkable similarity. Particularly in the equatorial tropical Pacific, specification of SSTs, via air–sea interactions, is able to generate the

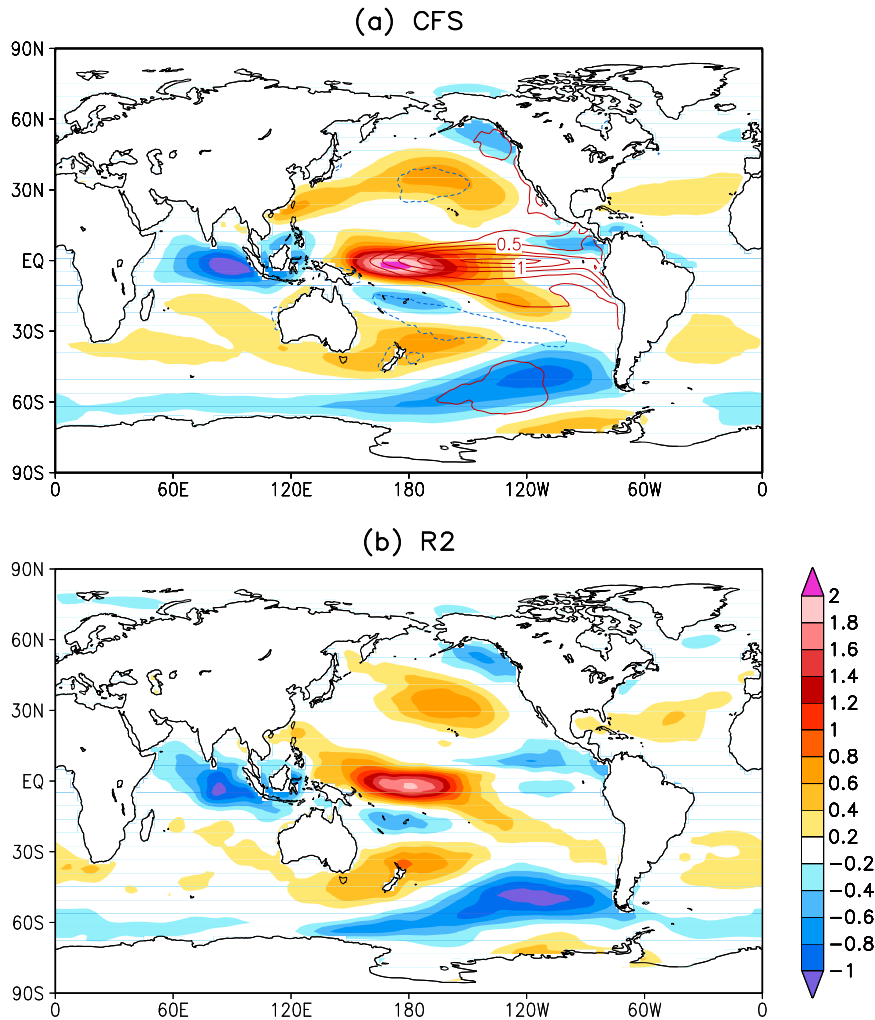


FIG. 3. Regression coefficient of SST vs Niño-3.4 SST index (contour, unit: K K^{-1}). The contour interval is 0.25 K K^{-1} with red solid (blue dash) contours for positive (negative) values; the zero contour is omitted. Regression coefficient of 10-m zonal wind vs Niño-3.4 SST index (shaded, unit: $\text{m s}^{-1} \text{ K}^{-1}$). (top) CFS and (bottom) R2.

observed structures in zonal wind in response to ENSO variability.

The analysis is encouraging in that in our design of model simulations, specification of SSTs via nudging is able to generate a surface zonal wind response to El Niño that is similar to that in observations. The results discussed so far, however, only illustrate statistical relationship between Niño-3.4 SST and zonal wind, and do not investigate temporal coherency between evolution of observed and model simulated zonal wind. For specification of SSTs to be able to simulate the observed evolution of subsurface ocean structure mediated through changes in surface winds, it is also important to compare temporal evolution of model-simulated zonal winds with observations. This is done based on the anomaly

correlation between the observed and model-simulated zonal winds, and spatial structure of temporal correlation, which is shown in Fig. 4 (top panel). We point out that temporal correlation is computed based on ensemble mean of model simulations to reduce the influence of noise and to maximize the anomaly correlation (Kumar and Hoerling 1995). The spatial structure of anomaly correlation based on individual runs, and then averaged over nine different simulations (not shown), is very similar to that shown in Fig. 4, but as expected, has smaller amplitude.

Consistent with the spatial structure of the SNR (Fig. 2) and regression with Niño-3.4 SST index (Fig. 3), the largest anomaly correlations are located over the tropical oceans, and further, over the equatorial tropical Pacific

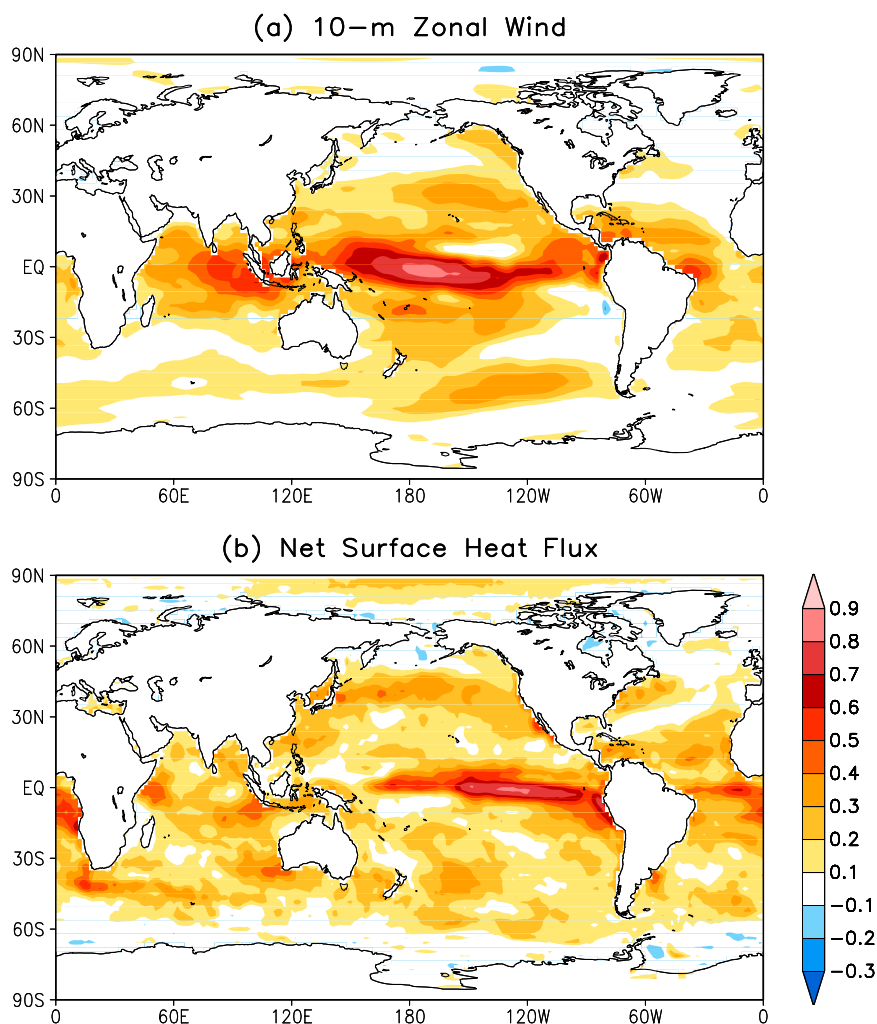


FIG. 4. Anomaly correlation for (a) 10-m zonal wind and (b) net surface heat flux between the ensemble mean of CFS simulations and R2 based on monthly mean data over 1981–2011.

where the largest value exceeds 0.8. Over the extratropical latitudes where SNR and regression analysis indicate far less constraint on zonal wind due to ENSO SST variability (or for that matter, due to any SSTs as the SNR analysis does not key on ENSO SST alone), the atmospheric internal variability dominates and temporal coherency between observations and model simulations is small.

For the sake of completeness, along with the anomaly correlation for surface wind, in Fig. 4 (bottom panel) we also show the anomaly correlation for the net heat flux at the ocean surface. Net heat flux is another component related to air–sea interaction that can influence subsurface ocean variability via changes in vertical stratification. In contrast to that for the surface wind, the largest anomaly correlation for net heat flux is shifted eastward. An eastward shift is consistent with the documented influence of ENSO on net flux variability

(e.g., see Fig. 8 in Kumar and Hu 2012) and is a consequence of changes in the latent and shortwave flux associated with ENSO.

As a further test of the ability of specified SSTs to simulate the observed surface zonal wind variability, Hovmöller diagrams of zonal wind at the equator are shown in Fig. 5. The left two panels compare the ensemble mean of model-simulated 10-m zonal wind with its observed counterpart. There is a remarkable similarity between the two over the equatorial Pacific. Because model results are based on ensemble means, their temporal evolution is smoother than the observations; however, all major features (including eastward propagation from western Pacific toward date line) are well replicated, and temporal correspondence also extends over to the eastern Indian Ocean where regression indicates a response over this region (Fig. 3).

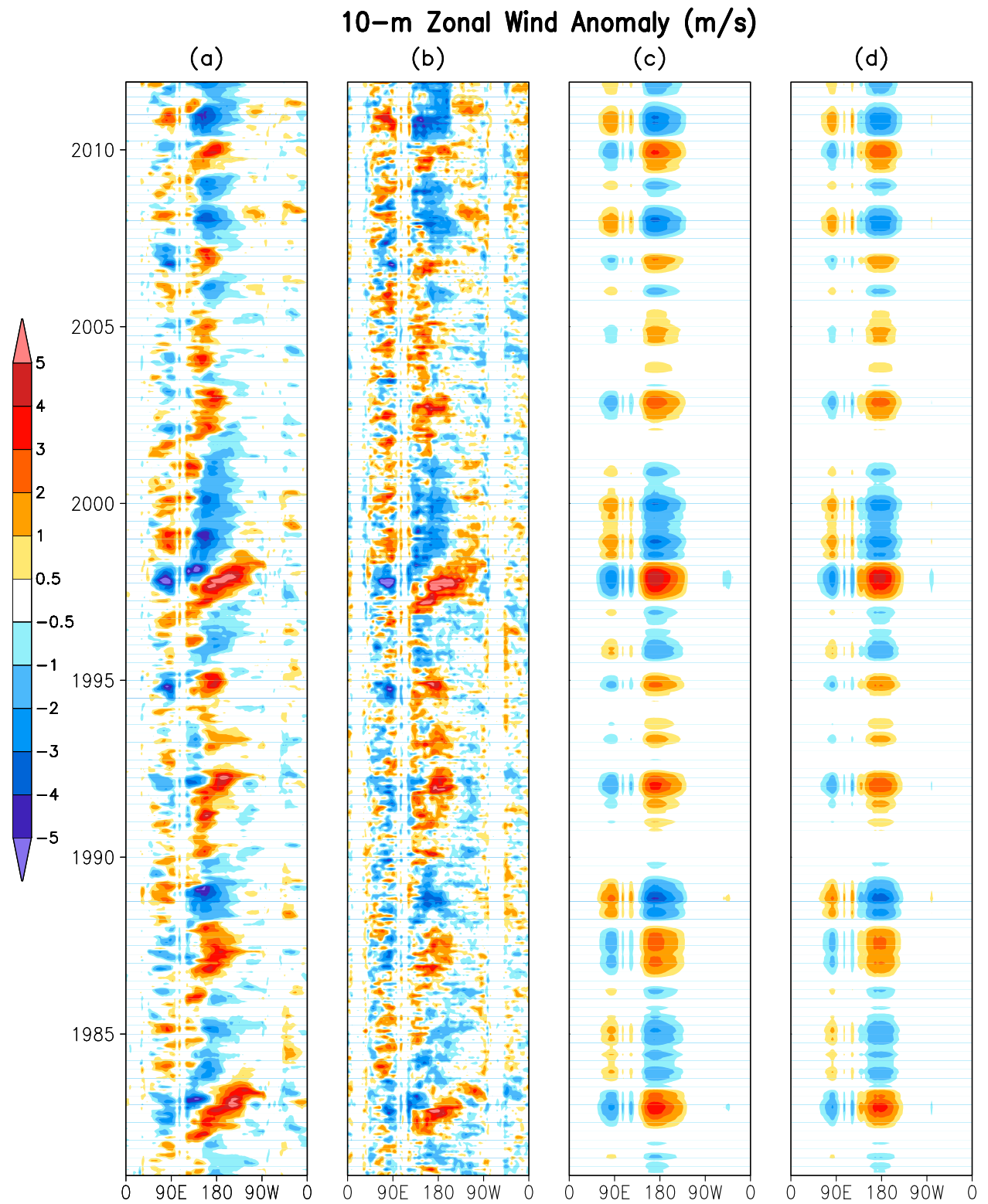


FIG. 5. 10-m zonal wind anomaly at the equator (unit: m s^{-1}): (a) ensemble mean of CFS simulations, (b) R2, (c) CFS reconstructed, and (d) R2 reconstructed. Reconstruction is based on regression with the Niño-3.4 SST index shown in Fig. 3.

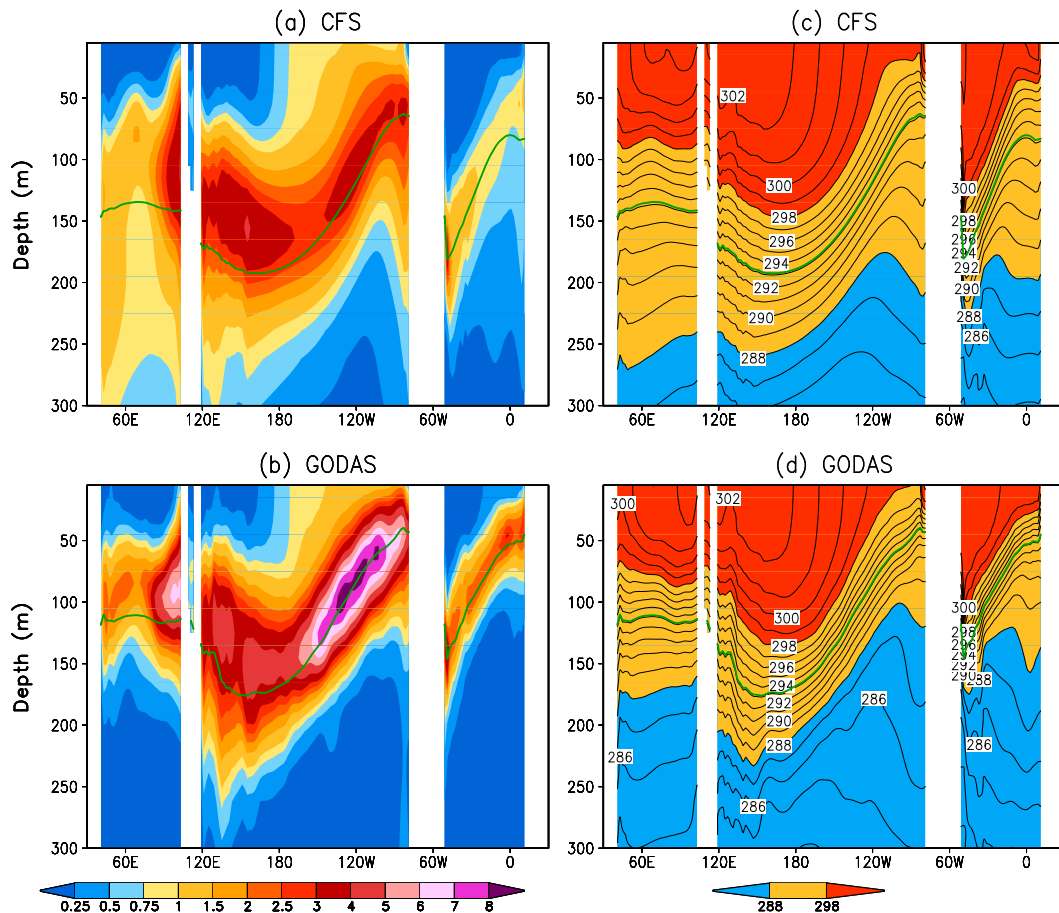


FIG. 6. (left) Variance (unit: K^2) and (right) long-term mean (unit: K) of subsurface ocean temperature averaged between $5^{\circ}S$ and $5^{\circ}N$ in (a),(c) CFS and (b),(d) GODAS. The green line is the $20^{\circ}C$ isotherm.

The two right panels in Fig. 5 compare the reconstructed zonal wind based on Niño-3.4 SST index regressions in Fig. 3. It is remarkable to note that the temporal evolution of all observed features is captured by the model simulations both over the equatorial tropical Pacific and over the eastern Indian Ocean. The comparison of 10-m zonal wind between model simulations and the observations, therefore, indicates that specification of SSTs is successful in replicating the observed wind variability associated with ENSO SST variations. Given that one of the primary causes of variability in the ocean is the adjustment to surface winds, this provides hope that observed variability in subsurface ocean temperatures may also be simulated to some extent, and is next analyzed.

Over the equatorial latitudes and averaged between $5^{\circ}S$ and $5^{\circ}N$ the monthly mean variability in ocean temperature for model simulations and observations based on GODAS is shown in Fig. 6 (left panels). Also shown with the green line is the $20^{\circ}C$ isotherm, which is a good representation of the mean thermocline in the tropics.

In the western Pacific the mean depth of thermocline is well simulated. In the eastern Pacific, however, the model-simulated mean thermocline is deeper than in the GODAS and the specification of SST observations alone is not sufficient to constrain the vertical structure of ocean temperature. A deeper thermocline in the eastern Pacific results from a too diffusive vertical temperature gradient in the model (Fig. 6, right panels). Over the Indian Ocean the mean depth of the thermocline is deeper than in the observed and is likely related to model biases as surface wind variability is not well constrained by specification of SSTs, and the ocean is free to evolve toward the state preferred by the model climatology. Over the Atlantic Ocean the east-west structure of the mean thermocline is well simulated but similar to that in eastern Pacific the model-simulated mean thermocline is deeper than in the observed, and once again is related to a too diffusive vertical temperature gradient.

The overall zonal and vertical structure of monthly mean ocean temperature variability is well replicated in

model simulations—larger values over the eastern Indian Ocean, east–west gradient in the depth of largest temperature variations over Pacific with larger variability in deeper (shallower) oceans in western (eastern) Pacific, and a similar east–west gradient in temperature variability over the Atlantic.

A notable discrepancy between model simulations and observations is weaker amplitude of variability, particularly in the eastern equatorial Pacific. This discrepancy is not related to the errors in the GODAS as a comparison with the ECMWF SYS4 ocean reanalysis (Balmaseda et al. 2013) (not shown) also shows the same feature. Possible reasons for the differences in the amplitude could be related to (i) a too diffuse thermocline in the eastern Pacific in model simulations (Fig. 6, right panels) that would also result in smaller variations in temperature in the vertical, or (ii) lack of submonthly surface wind variability in model simulations leading to weaker variations along the thermocline. A validation of the latter possibility is not pursued any further although the overall monthly mean variability of zonal winds in the model simulations indicates that variability of monthly mean zonal wind is in fact larger than for observations (Fig. 1).

Similar to that for 10-m zonal wind, the SNR for ocean temperatures in model simulations is shown in Fig. 7 (top panel), and highlights the amplitude of variability that is associated with specification of SSTs. Over the Pacific Ocean, the largest SNR is located near the surface and east of the date line, and decreases with depth. An analysis of individual components of variance related to signal and noise shows that for each component the largest variability is along the thermocline (Fig. 7, middle and bottom panels). Since away from the thermocline, in the upper ocean, for example, noise variance is quite small, it leads to the spatial structure of the SNR with smaller values along the thermocline and larger values above and below. There are also very large values for the SNR over some regions in the deeper oceans. A more detailed analysis shows that these are related to the initial drift in the ocean temperatures that is common to all model simulations that were initialized from the GODAS ocean initial condition, but in the absence of the ingest of ocean data, tend to drift toward model mean state (not shown). Further, as will be discussed next, another indication of this is that large SNRs in deeper oceans, unlike their surface counterpart, are not associated with ENSO variability.

The linear correlation and regression of subsurface ocean temperature between model simulations and GODAS with the Niño-3.4 SST index is compared in Fig. 8. This analysis mimics that for 10-m zonal wind (Fig. 3) and allows a comparison of linear response to

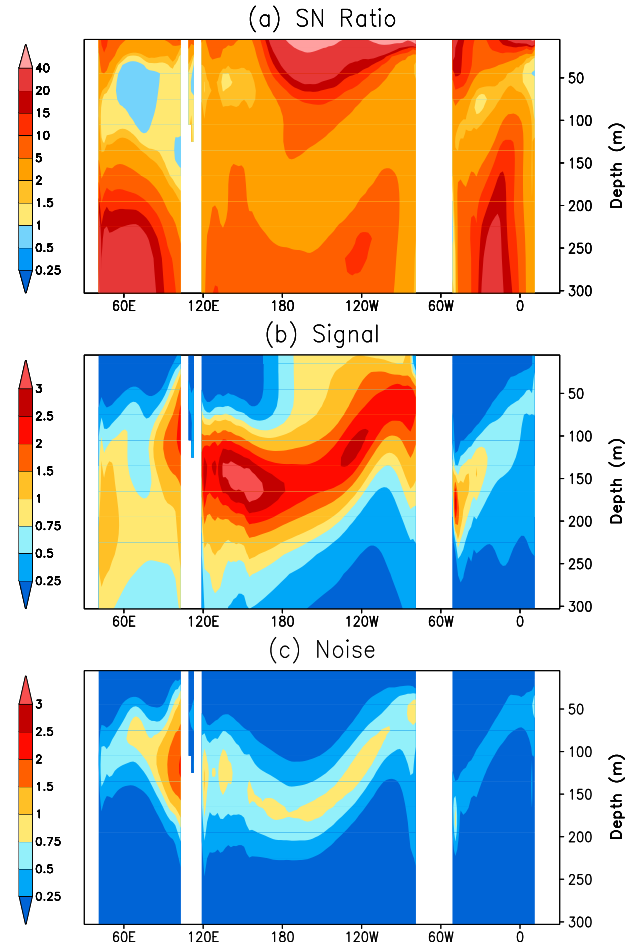


FIG. 7. Vertical-longitude cross sections of (a) signal-to-noise ratio, (b) signal (external variance; unit: K^2), and (c) noise (internal variance) of the subsurface temperature averaged between $5^{\circ}S$ and $5^{\circ}N$ derived from the CFS simulations.

ENSO in subsurface ocean temperature. The largest correlations with the Niño-3.4 SST index are over the tropical Pacific and show an east–west dipole structure that is reminiscent of the leading mode of subsurface ocean temperature variability associated with ENSO (Kumar and Hu 2014). In the eastern (western) Pacific the largest correlations are at the surface (~ 100 – 150 -m depth) and have a similar structure. There are no discernible signals associated with ENSO over the Atlantic, while over the Indian Ocean the largest correlation is over the eastern part and is likely in response to surface zonal wind variations over the same region (Fig. 3) leading to thermocline variations in the eastern component of the Indian Ocean dipole (IOD; Saji et al. 1999).

The regression pattern over the Pacific shows the largest amplitude along the thermocline (Fig. 8, bottom panel) and is consistent with the structure of signal variance (Fig. 7, middle panel) that is also largest along

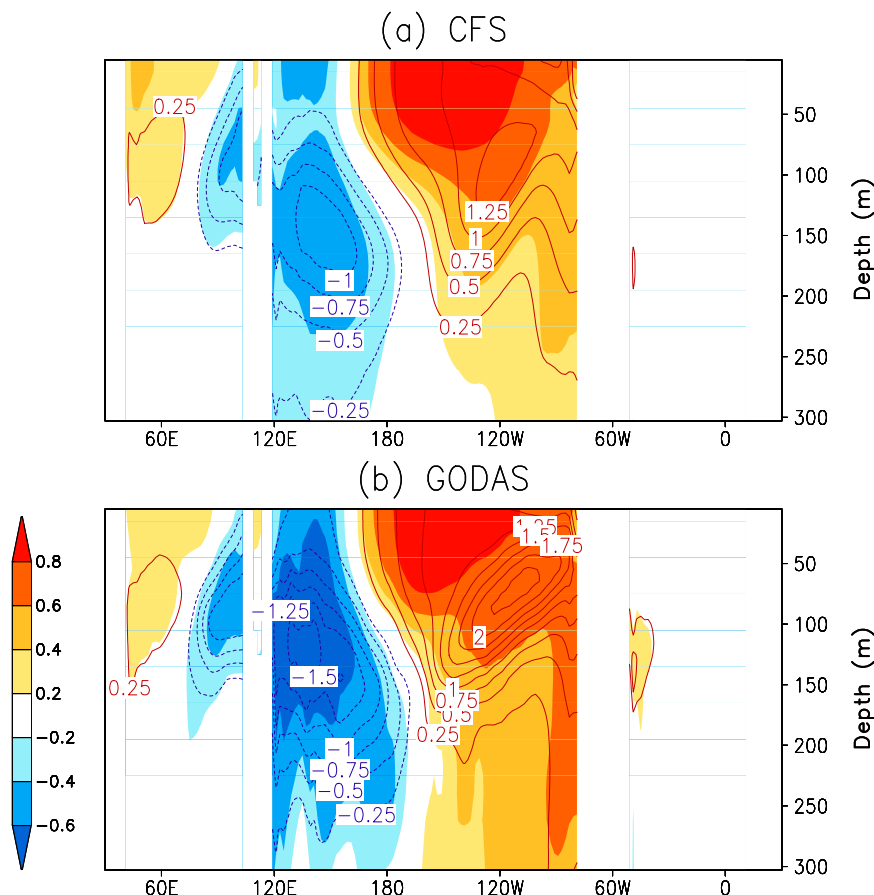


FIG. 8. Vertical-longitude cross sections of correlation (shadings) and regression coefficient (contour, unit: K K^{-1}) of the subsurface temperature anomalies vs Niño-3.4 index in (a) the CFS simulations and (c) GODAS averaged between 5°S and 5°N . The correlation in (a) is the average of correlations with nine individual CFS runs.

the thermocline. Similar to differences in monthly mean variance (Fig. 6), regression for the model simulation with ENSO is weaker, and in the eastern Pacific the maximum is located deeper in the ocean with more diffusive vertical gradient consistent with errors in the vertical structure of simulated ocean temperatures (Fig. 6, right panels). The amplitude of the correlation or the regression in deeper oceans (depth > 250 m) becomes very small, indicating that the large SNR in Fig. 7 (top panel) is not associated with ENSO SST variability.

In Fig. 9 the meridional cross sections of SNR, correlation, and regression with the Niño-3.4 SST index averaged between (Fig. 9a) $145^{\circ}\text{--}175^{\circ}\text{E}$, (Fig. 9b) the date line and 150°W , and (Fig. 9c) $105^{\circ}\text{--}135^{\circ}\text{W}$ are shown. Averages over these longitudes are chosen based on the ENSO influences on subsurface ocean temperatures (Fig. 8, bottom panel) which are located in deeper oceans for $145^{\circ}\text{--}175^{\circ}\text{E}$, are smallest between the date line and 150°W , and are closer to surface for the eastern region of

$105^{\circ}\text{--}135^{\circ}\text{W}$. Similar to their structure in longitudinal direction (Fig. 7), for all three locations the largest SNR values are at the surface. As mentioned earlier, larger values in deeper oceans for the SNR at all three locations are due to the initial drift in the model and are not related to ENSO variability (Fig. 9, bottom panels).

Both for correlation and regression patterns there is a good resemblance between model simulations and GODAS. For zonal average over $145^{\circ}\text{--}175^{\circ}\text{E}$ (Fig. 9, left column) response to ENSO SSTs is for negative ocean temperature anomalies and reflects the vertically elevated (depressed) thermocline during El Niño (La Niña) events. For the region near the date line (Fig. 9, middle column) positive correlations at the equator are flanked by negative correlations around 30° latitude in both hemispheres and collocated with a signature in surface zonal wind (Fig. 3). For the easternmost region of $105^{\circ}\text{--}135^{\circ}\text{W}$, a positive thermal response reflected as a deeper (shallower) thermocline during La Niña (El Niño) is

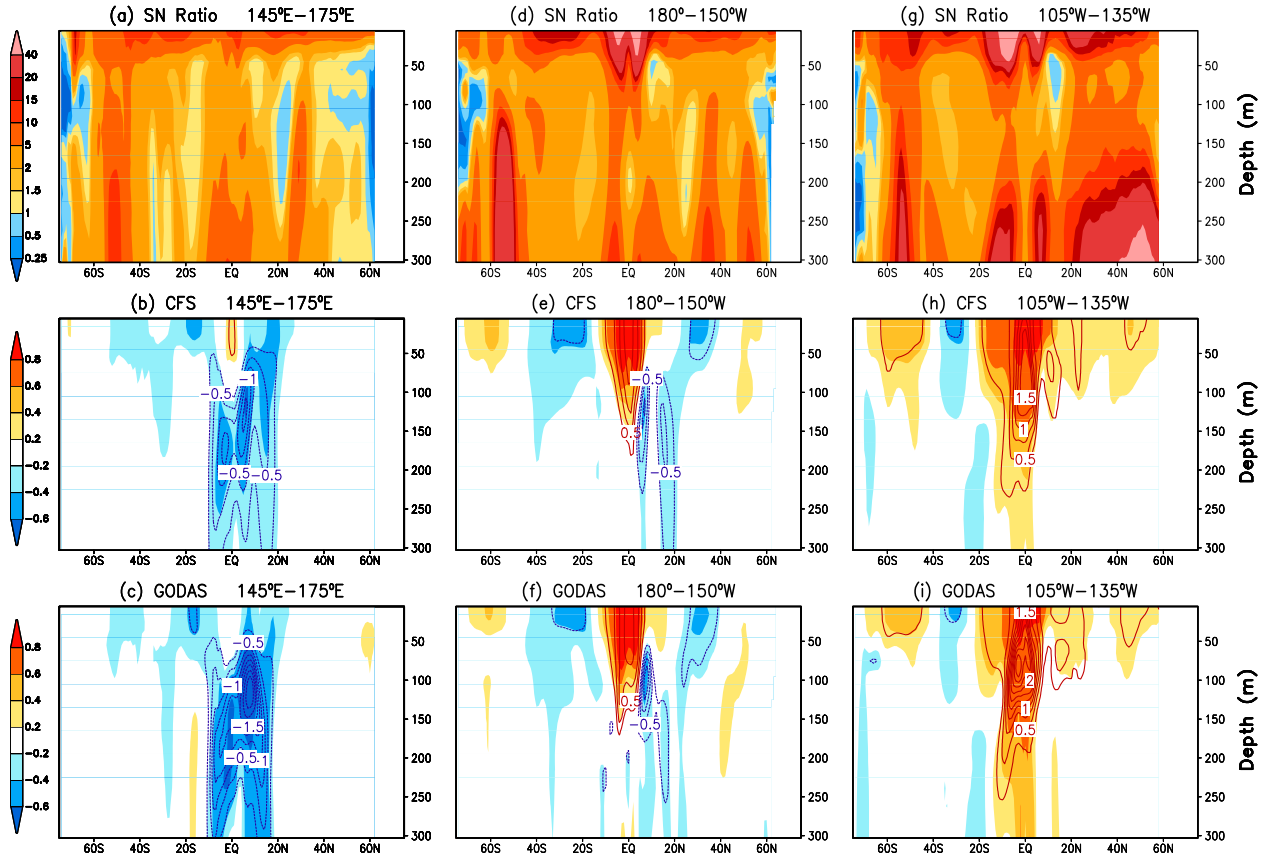


FIG. 9. Vertical–latitude cross sections of (a),(d),(g) signal-to-noise ratio in the subsurface monthly mean temperature; and correlation (shadings) and regression coefficient (contour, unit: K K^{-1}) of the subsurface temperature anomalies vs Niño-3.4 index in (b),(e),(h) the CFS simulations and (c),(f),(i) GODAS averaged between (left) 145° and 175°E , (middle) 180° and 150°W , and (right) 105° and 135°W . The correlation for the CFS in (b),(e),(h) is the average of correlations of nine individual CFS runs.

found. Further, consistent with the shallower mean thermocline over the eastern Pacific, the thermal response is also closer to surface. In the immediate vicinity of equatorial latitudes, the ENSO response also extends to deeper oceans and is due to ENSO's influence on equatorial ocean undercurrents.

The temporal coherence between the evolution of model-simulated and observed monthly mean temperature is shown in Fig. 10 (top panel). The largest correlations exceeding 0.9 are found over the Pacific Ocean near the date line and extend eastward. Larger values around 0.8 are also located in western Pacific at 150-m depth and correspond to the western pole of the dipole variability in equatorial ocean temperature associated with ENSO. Positive correlations are also found over the Indian and Atlantic Oceans, consistent with the depth of mean thermocline, but do not penetrate as deep in the ocean as over the Pacific.

For the GODAS, subsurface temperature observations are assimilated and the ocean current adjusts to them. Further, as a continual adjustment of thermal

structure toward the observed data that can also lead to discontinuities in ocean current, one would expect a much weaker correlation for the zonal current between model simulations and GODAS. This is indeed the case (Fig. 10, bottom panel), however, it is encouraging that correlations, even though weaker, are positive.

The analysis of variability in subsurface ocean temperature in model simulations indicates that specification of SST alone is capable of generating the observed subsurface ocean variability in equatorial latitudes. This is particularly true over the tropical Pacific. The connection between SST and subsurface ocean temperatures comes from the coupled air–sea interactions whereby (i) specified SSTs lead to modulation of low-level surface winds, and (ii) changes in surface wind lead to ocean adjustments and subsurface signature in temperature. That the proposed mechanism has validity comes from the result that it is over the equatorial tropical Pacific where air–sea coupled interactions are strongest; variations in the subsurface temperature variability are in phase with their observational counterpart. The

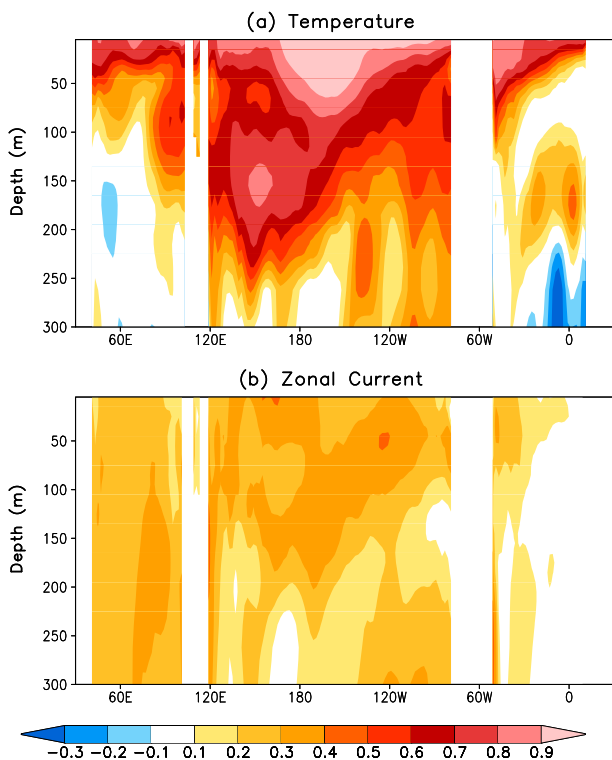


FIG. 10. Anomaly correlation for (a) subsurface ocean temperature and (b) zonal current between the ensemble mean of CFS simulations and R2 based on monthly mean data over 1981–2011. The correlations are averaged between 5°S and 5°N.

same mechanism has been the rationale for hybrid coupled models (Barnett et al. 1993), and the success of ENSO prediction efforts where the ocean initialization is achieved by relaxing SSTs in a freely evolving coupled model to the observed state (Chen et al. 2004; Luo et al. 2008; Keenlyside et al. 2008).

4. Discussion from the perspective of ocean observing system and data assimilation

In this section we provide some additional analysis and discussion from the perspective of the ocean observing system and data assimilation. In addition to relaxation to observed SSTs and specification of surface heat flux and momentum forcings (Behringer and Xue 2004) from R2, the ocean analysis in the GODAS is a consequence of the ingest of observations in deeper oceans (e.g., TAO moorings; Argo). A comparison of subsurface ocean temperature variability in model simulations with GODAS can also be interpreted as the influence of additional information due to ingest of the observational data. If the GODAS ocean analysis is considered to be the truth, and model simulations as one of the simplest assimilation (in which no subsurface

ocean data are assimilated and no surface forcing from atmospheric reanalysis is included) in a hierarchical complexity of assimilations, then discrepancies between the two could be interpreted as the contribution of subsurface ocean and atmosphere observations (through surface forcing) to the analyzed ocean state; and areas with low correlation in Fig. 10 would be indicative of regions where specification of SSTs as the only observation is not enough to constrain the ocean variability to the observed state (i.e., the GODAS).

An added level of complexity in this analysis, however, is the low-frequency variations in the characteristics of ENSO, particularly a shift in the characteristics of El Niño events (the warm phase of ENSO) from eastern Pacific events to central Pacific events after 2000 (McPhaden 2012; Luo et al. 2012; Hu et al. 2013). Such a shift, by changing surface wind variability and related ocean adjustment, may also lead to changes in the relationship in subsurface ocean temperatures between model simulations and the GODAS, and may overshadow fingerprints due to the evolving ocean observing system.

In this interpretation of SST-forced model simulations, correlation shown in Fig. 10 implies that specification (or assimilation) of SST is adequate for simulating the observed ocean temperature variability in the upper ocean near the date line. In the eastern Pacific where correlations are low, however, the observed SST variability is inadequate to constrain the ocean variability. Similarly in the deeper ocean below 200 m, constraint provided by SST is inadequate to simulate observed variability, although it should be noted that the amplitude of monthly mean temperature is also much weaker (Fig. 6).

The equatorial ocean observing system has been evolving with time (Saha et al. 2010), and it is of interest to analyze if this has any influence on the relationship between model simulations and the GODAS ocean analysis. In this part we only focus on the analysis in the tropical Pacific and show the results at discrete longitudes at the equator that sample regions of high and low correlations in Fig. 10. The analysis is based on the correlation between model-simulated and observed ocean temperature done over 5-yr moving window, and results are shown in Fig. 11. We note that although the interpretation of results in terms of the influence of the ocean observing system is not as straightforward as we had originally hoped for, results nonetheless have some interesting aspects.

In Fig. 11, correlations over four locations at the equator starting from the date line moving eastward are shown. Correlation over the entire period in Fig. 10 indicates that it is maximum at 150°W and decreases with longitudes farther east. At all four locations the

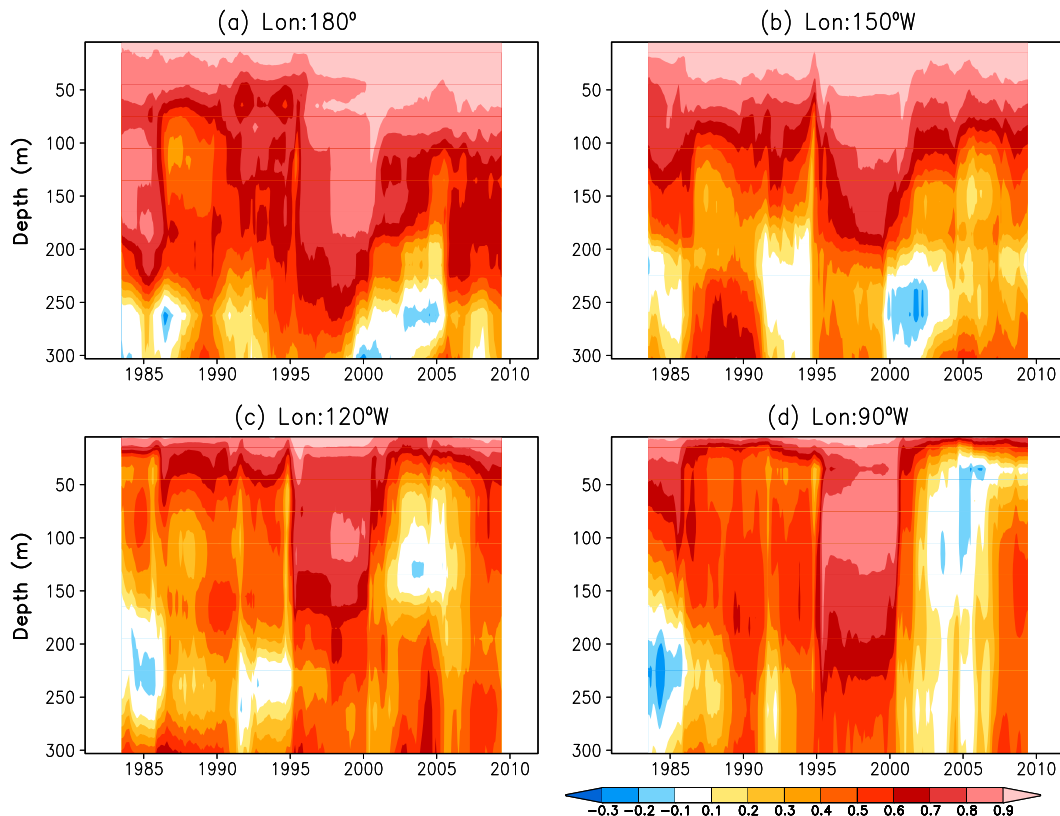


FIG. 11. Temporal anomaly correlation for ocean temperature between the CFS nine-member ensemble mean and GODAS for 5-yr moving windows at the equator but different longitudes: (a) 180°, (b) 150°W, (c) 120°W, and (d) 90°W.

correlations over the 5-yr sliding window are strongest centered about 1998 associated with the strongest El Niño during the analysis period. As will be shown later, this is due to the stronger surface wind response to SST anomalies. Some other interesting features in Fig. 11 include the following: at the date line, higher correlations are found over a deeper layer in the upper ocean continuing beyond 1998; visually there does not seem to be a systematic difference in correlations at 150°W before and after 1998; for locations farther east (120° and 90°W) there is a clear reduction in correlation with depth.

There have been considerable changes in the ocean observing system over the analysis period (Saha et al. 2010)—placement of TAO moorings starting 1990 and the commencement of Argo floats after 2000. If the ocean model used in the GODAS and model simulations is the same (as is the case for our analysis) intuitively one would expect that during the period of sparse data, temperature variability in SST-forced model simulations will be closer to that of GODAS since both are less constrained by observational data. As more and more subsurface data get assimilated, the GODAS correlation will get smaller. Changes in correlations,

however, do not entirely conform to this expectation: an increase in correlation at the date line after 2000 is contrary to this expectation; results are inconclusive at 150°W; and maybe, are in line with expectation at 120° and 90°W, where after the introduction of Argo, correlations are smaller.

A complicating factor in relating changes in correlation and its connection with the evolving observing system is the influence of low-frequency variability in ENSO. This is indicated by the fact that the largest correlations occur around 1998 influenced by ENSO, and similarly, a low-frequency changes in ENSO can easily overshadow the signature associated with changes in the ocean observing system. Indeed it has been documented that the character of ENSO variability in the tropical Pacific may have seen a shift after 2000, a period that also coincides with an increase in observations from Argo. At the ocean surface the shift is manifested as preponderance of central Pacific ENSO events (Yeh et al. 2009), which also have smaller amplitude. This westward shift and weaker amplitude in ENSO events may also be responsible for specification of SSTs in providing a weak constraint on the subsurface

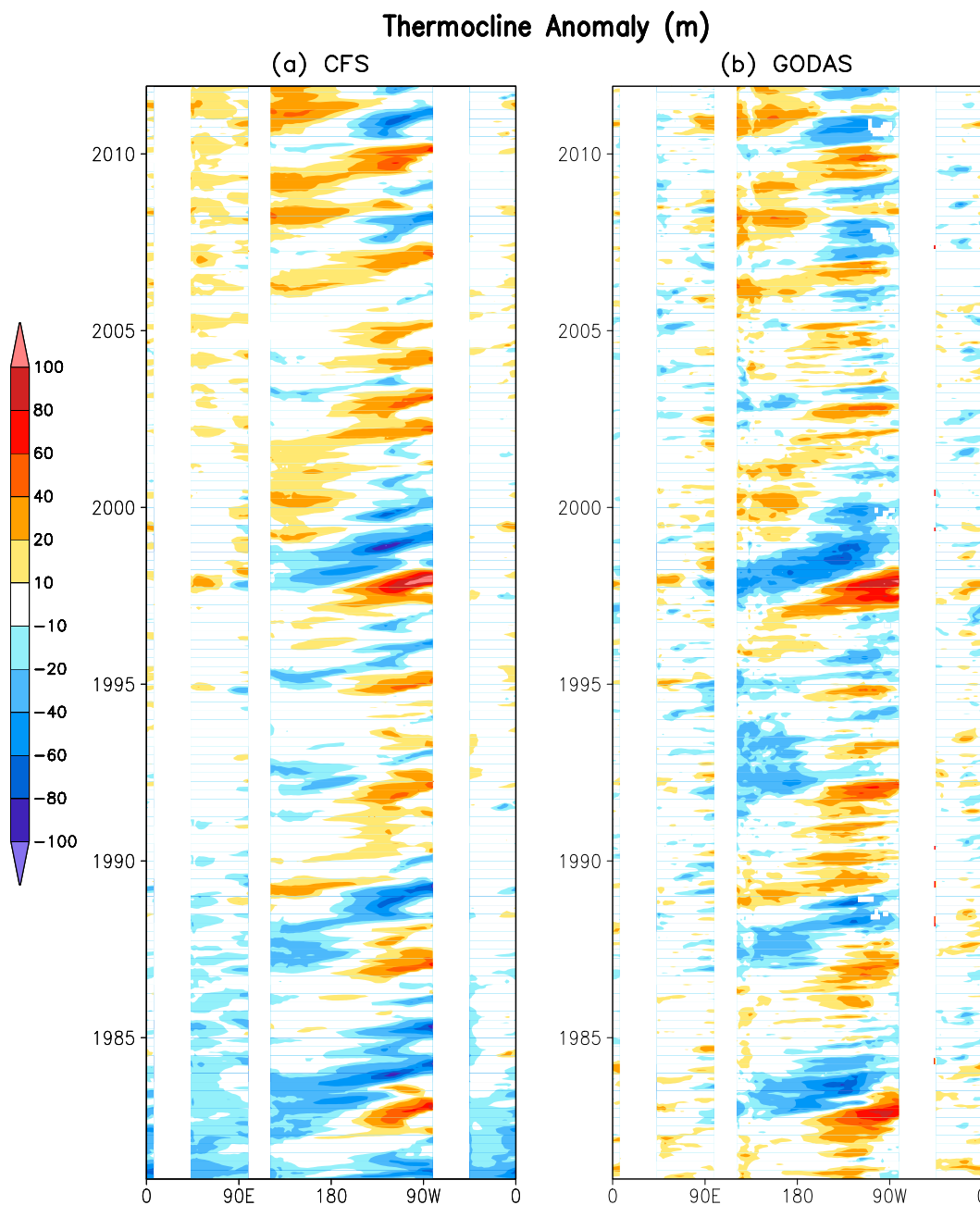


FIG. 12. Thermocline anomaly at the equator (unit: m) for (a) ensemble mean of CFS simulations and (b) GODAS. The depth of the thermocline is derived based on the depth of the 20°C isotherm.

ocean temperature evolution leading to lower correlation at 120° and 90°W after 2000. A westward shift in SST could also explain increased correlation at the date line as this may now fall east of the surface zonal wind response to central Pacific ENSO events.

A change in the characteristics of ENSO variability after 2000 is aptly captured by variability in thermocline. Figure 12 illustrates the longitudinal variations in

thermocline similar to that for surface wind in Fig. 5. Before 2000, both model simulations and the GODAS strongest variations in thermocline are located in the eastern Pacific and have good temporal coherence. After 2000, however, larger amplitude variations in thermocline shift toward the central Pacific, and further, the characteristics of the thermocline variability in the eastern Pacific shift toward higher-frequency variations. This

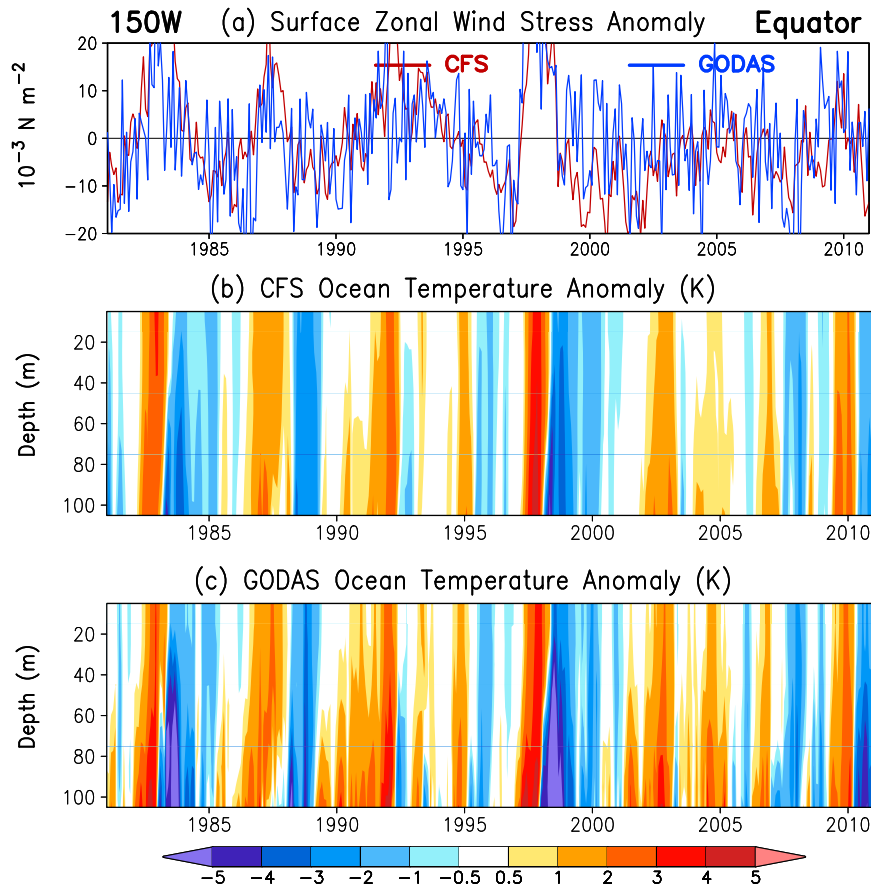


FIG. 13. (a) Time series of surface zonal wind stress anomaly (unit: 10^{-3} N m^{-2} , red: CFS, blue: GODAS), and depth–time diagrams of subsurface ocean temperature anomalies at (150°W , equator) from (b) the ensemble mean of the CFS simulations and (c) GODAS.

change in the characteristics of ENSO after 2000 may be responsible for the breakdown in the correlation of subsurface ocean temperature after 2000 (Fig. 11) for the eastern part of the Pacific basin.

To further highlight the possible influence of low-frequency variability in ENSO, we show the temporal evolution of 10-m zonal wind, and ocean temperatures at 150°W (Fig. 13) and 90°W (Fig. 14). Consistent with the correlation in Figs. 10 and 11, the observed variations in subsurface ocean temperature at 150°W are well reproduced in model simulations, and it is indeed remarkable that specification of SST alone can generate such a level of realism. The evolution also indicates a clear change in characteristics of ENSO across 2000: stronger and longer-lasting ENSO events before 2000; lower-frequency variations in surface zonal wind before 2000 that are well reproduced; after 2000 zonal wind to have a tendency to be in the easterly phase, a fact noted in earlier studies (Xiang et al. 2013; Luo et al. 2012). The time series also illustrates that the amplitude of the influence of ENSO

variability alone in model simulations forced with SST is comparable to that in observations (see also Fig. 5), and can easily overwhelm a possible signature due to changes in the observing system. We should point out that model results are based on ensemble means, and therefore, have smoother variations.

At 90°W (Fig. 14) variations in zonal wind are much smaller in amplitude, and for observations, there is clear shift around 1998 toward an easterly phase and negative temperature anomalies. A similar change in the mean state in the equatorial Pacific was also noted by Hu et al. (2013). At this particular location in the far eastern Pacific, the observed ocean temperature variability has a clear signature of ENSO events before 2000. After 2000, variability shifts to a higher frequency and is no longer reproduced in model simulations leading to lower correlations (Fig. 11). In summary, in the analysis of correlations over 5-yr window, variability in ENSO by far dominates the potential fingerprint due to a change in the ocean observing system.

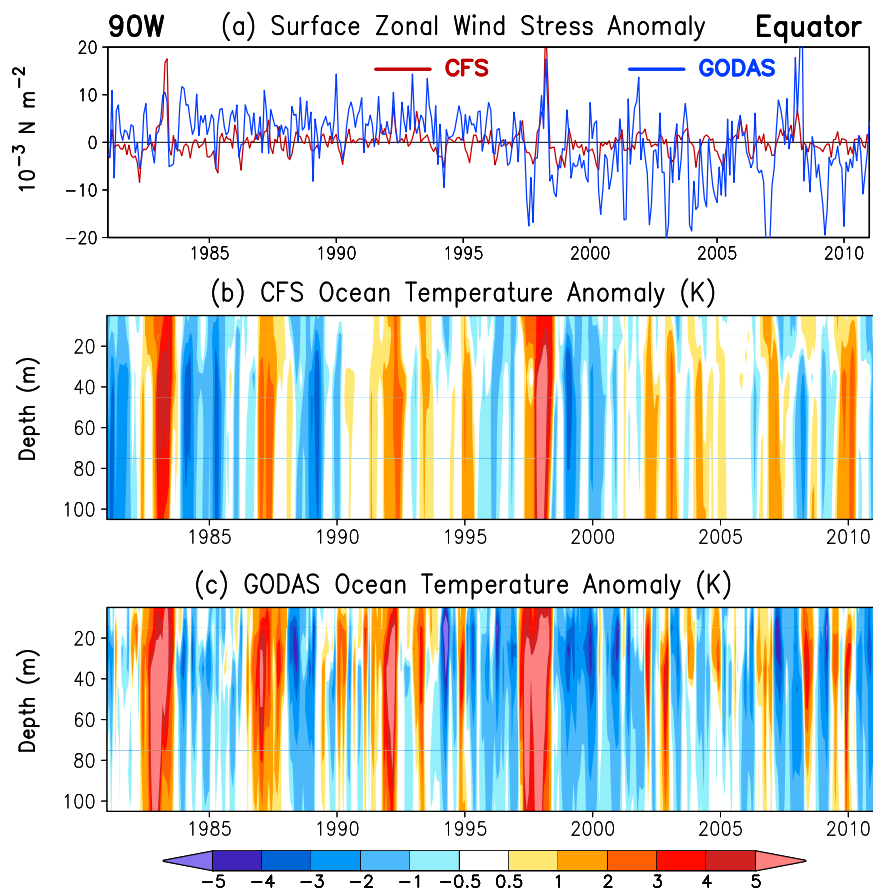


FIG. 14. (a) Time series of surface zonal wind stress anomaly (unit: 10^{-3} N m^{-2} , red: CFS, blue: GODAS), and depth–time diagrams of subsurface ocean temperature anomalies at (90°W , equator) from (b) the ensemble mean of the CFS simulations and (c) GODAS.

5. Summary and discussion

The focus of the analysis was to explore the question to what extent specification of SSTs in equatorial latitudes, particularly in the Pacific, can replicate the observed subsurface ocean temperature variability. The physical argument for such a possibility to exist is that SSTs, via coupled air–sea interaction, may lead to reasonable variations in surface winds and subsequent adjustment in the subsurface ocean state.

The results indicate that indeed the specification of SSTs, via coupled air–sea interaction, is able to generate subsurface ocean temperature variability. This is particularly true in the equatorial Pacific for ocean variability, and for variability associated with ENSO. To impress this fact further, Fig. 15 shows two leading modes of heat content variability in the upper 300 m of the oceans (referred to as HC300), and the corresponding time series are shown in Fig. 16. For model simulations EOFs are computed for each run separately and then averaged.

The first two leading modes of HC300 are associated with ENSO variability in the tropical Pacific with the first mode representing the east–west tilt in thermocline while the second mode is associated with the changes in the warm water volume (WWV) linked to recharge–discharge of equatorial heat content as dynamical response to changes in equatorial thermocline. The observed spatial structure of two modes of HC300 is well captured in model simulations. The time series (Fig. 16) comparison also shows that model simulations can well replicate the observed evolution. Discrepancy at the start of the time series in 1981 is because of initial spinup toward the model climatology when no subsurface ocean data are assimilated. This large spinup time, that even for the upper ocean exceeds a couple of years, should be considered in climate reanalysis systems that are run in multiple streams with an overlap to minimize discontinuities in the ocean analysis across different streams (Xue et al. 2012). In Fig. 16 for the time series of EOFs, one can also discern a phase delay of 1–2 months in the HC300 variability for the model simulations indicating the

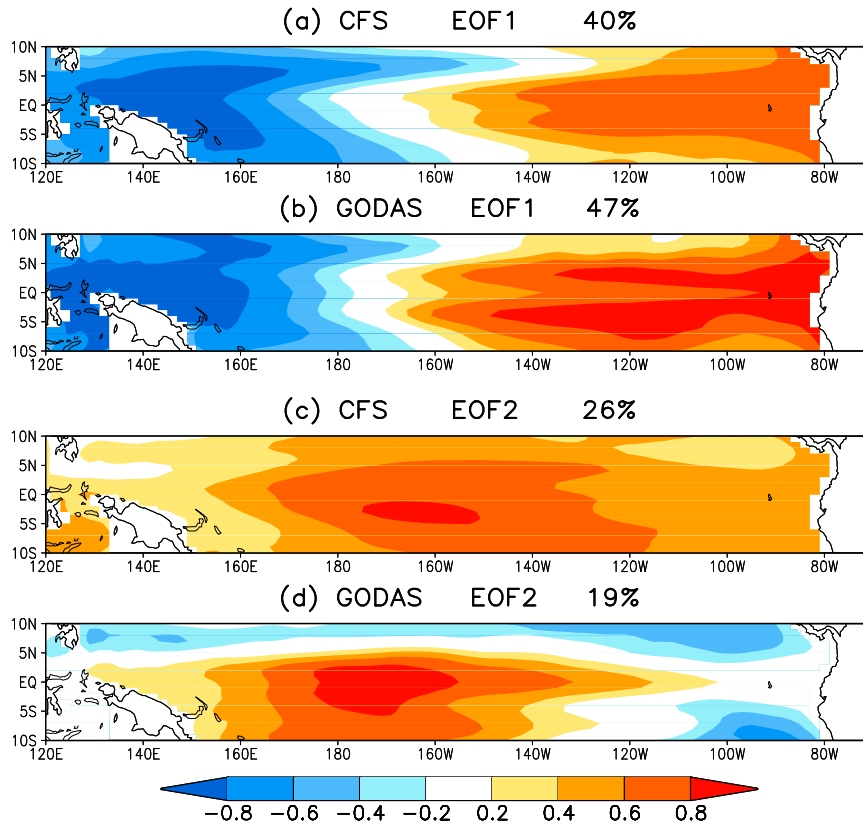


FIG. 15. Spatial patterns of the first two EOFs of the 300-m heat content in (a),(c) CFS and (b),(d) GODAS. The EOF analysis is performed in the domain of (10°S–10°N, 120°E–80°W). Maps are shown in correlations between 300-m heat content and the corresponding PC time series. For CFS, the correlations are first calculated for the nine individual members, and then averaged over the nine members. The percent of the total variance explained by each EOF is listed at the top of each panel.

possible influence of high-frequency atmospheric variability that cannot be captured in SST assimilation experiments alone. In summary, specification of SSTs alone in model simulations is able to capture the subsurface variability in ocean temperatures associated with ENSO, and may explain the success of ENSO prediction systems initialized with nudging the coupled model to observed SSTs.

In the context of the ocean observing system, and assuming GODAS ocean analysis to be the truth, the results have implications for the need for the ocean observing system to constrain analyzed ocean states. For example, in the tropical Pacific, the requirement for the ocean observing system may be much stronger in the eastern Pacific than in the central Pacific. This requirement, however, when evaluated in the context of skillful ENSO prediction may have a different perspective. For ENSO prediction thermocline variations in the central Pacific are of foremost importance and contain the ENSO memory. Therefore, even if the observing system

in the eastern Pacific may add to the accuracy of ocean conditions, it may not add to the skill of ENSO prediction. Demonstrating some of these caveats will require a controlled set of forecast experiments (Keenlyside et al. 2005; Zhu et al. 2012), where ocean initial conditions are obtained either from the SST-based ocean assimilation state or from the GODAS, and the skill of ENSO prediction is evaluated.

Regarding the ENSO prediction problem and the requirements for the observing system, the analysis also raises some intriguing questions. The model simulations with the specification of SSTs clearly indicate that ENSO-related variability in subsurface ocean temperature can be well replicated. The reason for this is strong air–sea coupling, which is also the basis for prediction skill of ENSO. Although not analyzed, it is likely that for the SST-forced assimilation even if the statistics of high-frequency events may be predictable (Luo et al. 2005), it is unlikely that the timing of such event can be predicted with long leads, and therefore, the SST assimilation run

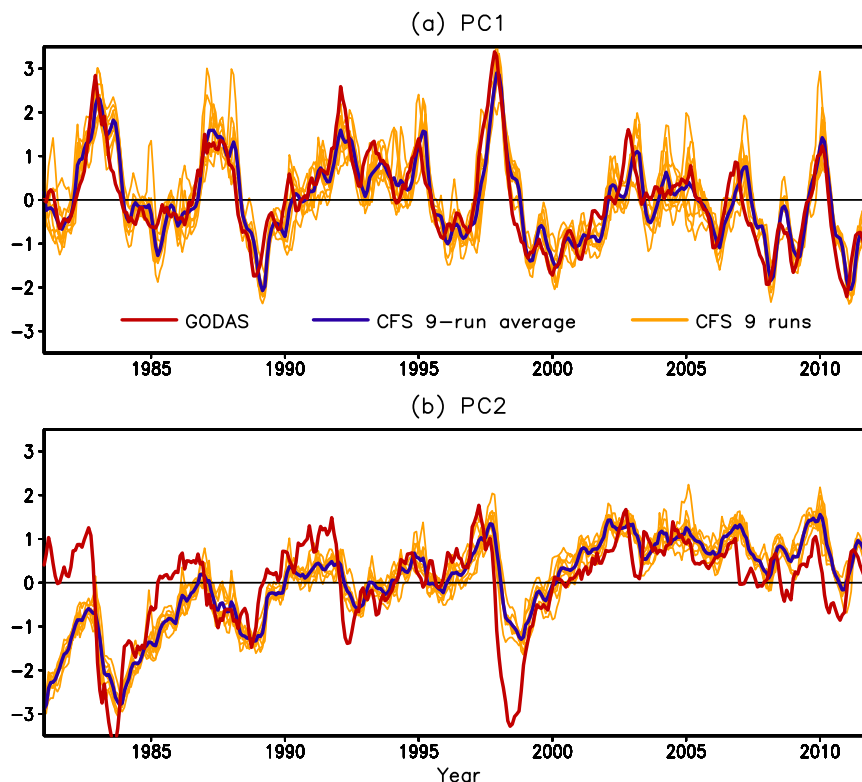


FIG. 16. Normalized monthly time series of (a) PC1 and (b) PC2 from 1981 to 2011 with red for GODAS, blue for CFS nine-member average, and yellow for the CFS nine individual members.

cannot resolve ocean response to high-frequency ocean variability related to the atmospheric internal variability—the Madden–Julian oscillation (MJO), westerly wind bursts, etc. These events, which are rarely predictable beyond couple of weeks, can have strong implications for the timing of initiation and termination of ENSO events and its amplitude (e.g., McPhaden 1999). These phenomena related to atmospheric internal variability, therefore, impart an unpredictable component to the long lead prediction of ENSO (Wang et al. 2011), and impose limits on the longer lead predictability of the timing and amplitude of ENSO.

Acknowledgments. We thank three anonymous reviewers and the editor for their constructive and insightful comments and suggestions.

REFERENCES

- Balmaseda, M. A., D. L. T. Anderson, and M. K. Davey, 1994: ENSO prediction using dynamical ocean model coupled to statistical atmosphere. *Tellus*, **46A**, 497–511.
- , K. Mogensen, and A. T. Weaver, 2013: Evaluation of the ECMWF ocean reanalysis system ORAS4. *Quart. J. Roy. Meteor. Soc.*, **139**, 1132–1161, doi:10.1002/qj.2063.
- Barnett, T. P., M. Latif, N. Graham, M. Flugel, S. Pazan, and W. White, 1993: ENSO and ENSO-related predictability. Part I: Prediction of equatorial Pacific sea surface temperature with a hybrid coupled ocean–atmosphere mode. *J. Climate*, **6**, 1545–1566.
- Behringer, D. W., and Y. Xue, 2004: Evaluation of the global ocean data assimilation system at NCEP: The Pacific Ocean. Preprints, *Eighth Symp. on Integrated Observing and Assimilation Systems for Atmosphere, Oceans, and Land Surface*, Seattle, WA, Amer. Meteor. Soc., 2.3. [Available online at http://ams.confex.com/ams/84Annual/techprogram/paper_70720.htm.]
- , M. Ji, and A. Leetmaa, 1998: An improved coupled model for ENSO prediction and implications for ocean initialization. Part I: The ocean data assimilation system. *Mon. Wea. Rev.*, **126**, 1013–1021.
- Blackmon, M. L., 1976: A climatological spectral study of the 500 mb geopotential height of the Northern Hemisphere. *J. Atmos. Sci.*, **33**, 1607–1623.
- Chen, D., M. A. Cane, A. Kaplan, S. E. Zebiak, and D. J. Huang, 2004: Predictability of El Niño over the past 148 years. *Nature*, **428**, 733–736.
- Chen, M., W. Wang, A. Kumar, H. Wang, and B. Jha, 2012: Ocean surface impacts on the seasonal-mean precipitation over the tropical Indian Ocean. *J. Climate*, **25**, 3566–3582.
- Deser, C., M. A. Alexander, S.-P. Xie, and A. S. Phillips, 2010: Sea surface temperature variability: Patterns and mechanisms. *Annu. Rev. Mar. Sci.*, **2**, 115–143.

- Hoerling, M. P., and A. Kumar, 1997: Origins of extreme climate states during the 1982–83 ENSO winter. *J. Climate*, **10**, 2859–2870.
- Horel, J. D., and J. M. Wallace, 1981: Planetary scale atmospheric phenomena associated with the Southern Oscillation. *Mon. Wea. Rev.*, **109**, 813–829.
- Hu, Z.-Z., A. Kumar, H. Ren, H. Wang, M. L'Heureux, and F.-F. Jin, 2013: Weakened interannual variability in the tropical Pacific Ocean since 2000. *J. Climate*, **26**, 2601–2613.
- Jin, E. K., and Coauthors, 2008: Current status of ENSO prediction skill in coupled ocean–atmosphere models. *Climate Dyn.*, **31**, 647–664.
- Kanamitsu, M., and Coauthors, 2002: NCEP dynamical seasonal forecast system 2000. *Bull. Amer. Meteor. Soc.*, **83**, 1019–1037.
- Keenlyside, N. S., M. Latif, M. Botzet, J. Jungclaus, and U. Schulzweida, 2005: A coupled method for initializing El Niño–Southern Oscillation forecasts using sea surface temperature, *Tellus*, **57A**, 340–356.
- , —, J. Jungclaus, L. Kornbluh, and E. Roeckner, 2008: Advancing decadal-scale climate prediction in the North Atlantic sector. *Nature*, **453**, 84–88.
- Kumar, A., and M. P. Hoerling, 1995: Prospects and limitations of atmospheric GCM climate predictions. *Bull. Amer. Meteor. Soc.*, **76**, 335–345.
- , and Z.-Z. Hu, 2012: Uncertainty in ocean–atmosphere feedbacks associated with ENSO in the reanalysis products. *Climate Dyn.*, **39**, 575–588.
- , and —, 2014: Interannual and interdecadal variability of ocean temperature along the equatorial Pacific in conjunction with ENSO. *Climate Dyn.*, doi:10.1007/s00382-013-1721-0, in press.
- , A. G. Barnston, and M. P. Hoerling, 2001: Seasonal predictions, probabilistic verifications, and ensemble size. *J. Climate*, **14**, 1671–1676.
- Latif, M., and A. Villwock, 1990: Interannual variability as simulated in coupled ocean–atmosphere models. *J. Mar. Syst.*, **1**, 51–60.
- Luo, J.-J., S. Masson, S. Behera, S. Shingu, and T. Yamagata, 2005: Seasonal climate predictability in a coupled OAGCM using a different approach for ensemble forecasts. *J. Climate*, **18**, 4474–4497.
- , —, —, and T. Yamagata, 2008: Extended ENSO predictions using a fully coupled ocean–atmosphere model. *J. Climate*, **21**, 84–93.
- , W. Sasaki, and Y. Masumoto, 2012: Indian Ocean warming modulates Pacific climate change. *Proc. Natl. Acad. Sci. USA*, **109**, 18 701–18 706, doi:10.1073/pnas.1210239109.
- McPhaden, M. J., 1999: Genesis and evolution of the 1997–98 El Niño. *Science*, **283**, 950–954.
- , 2012: A 21st century shift in the relationship between ENSO SST and warm water volume anomalies. *Geophys. Res. Lett.*, **39**, L09706, doi:10.1029/2012GL051826.
- Meehl, G. A., and Coauthors, 2014: Decadal climate prediction: An update from the trenches. *Bull. Amer. Meteor. Soc.*, in press.
- Moorthi, S., H.-L. Pan, and P. Caplan, 2001: Changes to the 2001 NCEP operational MRF/AVN global analysis/forecast system. NWS Tech. Procedures Bull. 484, 14 pp. [Available online at <http://www.nws.noaa.gov/om/tpb/484.htm>.]
- Oberhuber, J. M., E. Roeckner, M. Christoph, M. Esch, and M. Latif, 1998: Predicting the '97 El Niño event with a global climate model. *Geophys. Res. Lett.*, **25**, 2273–2276.
- Pacanowski, R. C., and S. M. Griffies, 1998: MOM 3.0 manual. NOAA/Geophysical Fluid Dynamics Laboratory, 668 pp.
- Pan, H.-L., and L. Mahrt, 1987: Interaction between soil hydrology and boundary layer developments. *Bound.-Layer Meteor.*, **38**, 185–202.
- Peng, P., A. Kumar, A. G. Barnston, and L. Goddard, 2000: Simulation skills of the SST-forced global climate variability of the NCEP-MRF9 and the Scripps–MPI ECHAM3 models. *J. Climate*, **13**, 3657–3679.
- , —, M. S. Halpert, and A. G. Barnston, 2012: An analysis of CPC's operational 0.5-month lead seasonal outlooks. *Wea. Forecasting*, **27**, 898–917.
- Reynolds, R. W., N. A. Rayner, T. M. Smith, D. C. Stokes, and W. Wang, 2002: An improved in situ and satellite SST analysis for climate. *J. Climate*, **15**, 1609–1625.
- Ropelewski, C. F., and M. S. Halpert, 1986: North American precipitation and temperature patterns associated with the El Niño/Southern Oscillation (ENSO). *Mon. Wea. Rev.*, **114**, 2352–2362.
- , and —, 1987: Global and regional scale precipitation patterns associated with the El Niño/Southern Oscillation. *Mon. Wea. Rev.*, **115**, 1606–1626.
- Saha, S., and Coauthors, 2006: The NCEP Climate Forecast System. *J. Climate*, **19**, 3483–3517.
- , and Coauthors, 2010: The NCEP Climate Forecast System Reanalysis. *Bull. Amer. Meteor. Soc.*, **91**, 1015–1057.
- , and Coauthors, 2014: The NCEP Climate Forecast System version 2. *J. Climate*, in press.
- Saji, N. H., B. N. Goswami, P. N. Vinayachandran, and T. Yamagata, 1999: A dipole mode in the tropical Indian Ocean. *Nature*, **401**, 360–363.
- Tang, Y., and R. Kleeman, 2004: SST assimilation experiments in a tropical Pacific Ocean model. *J. Phys. Oceanogr.*, **34**, 623–642.
- Trenberth, K. E., G. W. Branstator, D. J. Karoly, A. Kumar, N. C. Lau, and C. Ropelewski, 1998: Process during TOGA in understanding and modeling global teleconnections associated with tropical sea surface temperatures. *J. Geophys. Res.*, **103** (C7), 14 291–14 324.
- Wang, H., A. Kumar, and W. Wang, 2013: Characteristics of subsurface ocean response to ENSO assessed from simulations with the NCEP Climate Forecast System. *J. Climate*, **26**, 8065–8083.
- Wang, W., M. Chen, A. Kumar, and Y. Xue, 2011: How important is intraseasonal surface wind variability to real-time ENSO prediction? *Geophys. Res. Lett.*, **38**, L13705, doi:10.1029/2011GL047684.
- Xiang, B., B. Wang, and T. Li, 2013: A new paradigm for the predominance of standing central Pacific warming after the late 1990s. *Climate Dyn.*, **41**, 327–340, doi:10.1007/s00382-012-1427-8.
- Xue, Y., and Coauthors, 2012: A comparative analysis of upper-ocean heat content variability from an ensemble of operational ocean reanalyses. *J. Climate*, **25**, 6905–6929.
- , M. Chen, A. Kumar, Z.-Z. Hu, and W. Wang, 2013: Prediction skill and bias of tropical Pacific sea surface temperatures in the NCEP Climate Forecast System version 2. *J. Climate*, **26**, 5358–5378.
- Yeh, S.-W., J.-S. Kug, B. Dewitte, M.-H. Kwon, B. P. Kirtman, and F.-F. Jin, 2009: El Niño in a changing climate. *Nature*, **461**, 511–514.
- Zhu, J., B. Huang, L. Marx, J. L. Kinter III, M. A. Balmaseda, R.-H. Zhang, and Z.-Z. Hu, 2012: Ensemble ENSO hindcasts initialized from multiple ocean analyses. *Geophys. Res. Lett.*, **39**, L09602, doi:10.1029/2012GL051503.